PHYSICS

Spin fluctuation induced Weyl semimetal state in the paramagnetic phase of $EuCd_2As_2$

J.-Z. Ma[1,2]*, S. M. Nie[3]*, C. J. Yi[4,5]*, J. Jandke[1], T. Shang[1,2,6], M. Y. Yao[1], M. Naamneh[1], L. Q. Yan[4], Y. Sun[4,5,7], A. Chikina[1], V. N. Strocov[1], M. Medarde[6], M. Song[8,9], Y.-M. Xiong[8,10], G. Xu[11], W. Wulfhekel[12], J. Mesot[1,2,13], M. Reticcioli[14], C. Franchini[14,15], C. Mudry[16,17], M. Müller[16], Y. G. Shi[4,7†], T. Qian[4,7,18†], H. Ding[4,5,7,18], M. Shi[1†]

Weyl fermions as emergent quasiparticles can arise in Weyl semimetals (WSMs) in which the energy bands are nondegenerate, resulting from inversion or time-reversal symmetry breaking. Nevertheless, experimental evidence for magnetically induced WSMs is scarce. Here, using photoemission spectroscopy, we observe that the degeneracy of Bloch bands is already lifted in the paramagnetic phase of $EuCd_2As_2$. We attribute this effect to the itinerant electrons experiencing quasi-static and quasi–long-range ferromagnetic fluctuations. Moreover, the spin-nondegenerate band structure harbors a pair of ideal Weyl nodes near the Fermi level. Hence, we show that long-range magnetic order and the spontaneous breaking of time-reversal symmetry are not essential requirements for WSM states in centrosymmetric systems and that WSM states can emerge in a wider range of condensed matter systems than previously thought.

INTRODUCTION

In crystals, Kramers' theorem, together with the combination of inversion (P) and time reversal (T) symmetries, protects the double degeneracy of fermionic energy bands. Dirac nodes can emerge at the gapless crossing of two doubly degenerate bands, near which the fermionic excitations are described by the massless 4-by-4 Dirac equation (*1*–*4*). The twofold band degeneracy can be lifted when P or T symmetry is broken. The crossings of nondegenerate bands then lead to Weyl nodes that always occur in pairs. The electronic states with momenta close to a Weyl node are effectively governed by the 2-by-2 Weyl equation (*5*). While P symmetry breaking is explicitly present in noncentrosymmetric systems, T symmetry can be broken either explicitly by external magnetic fields or spontaneously through correlation effects. First-principles calculations have predicted a number of Weyl semimetals (WSMs) in noncentrosymmetric or magnetically ordered systems (*5*–*10*). From angle-resolved photoemission spectroscopy (ARPES) experiments, the Weyl nodes have been identified in several noncentrosymmetric systems, such as the TaAs family, (Mo,W)Te_2, LaAlGe, and $TaIrTe_4$ (*11*–*18*). By contrast, there is no well-defined spectroscopic evidence for Weyl nodes in magnetically ordered systems. Moreover, magnetotransport measurements have provided evidence for the chiral anomaly expected from Weyl fermions in TaAs, Na_3Bi, GdPtBi, Mn_3Sn, and $Co_3Sn_2S_2$ (*19*–*23*). The Weyl nodes in Na_3Bi and GdPtBi are created by external magnetic fields.

Here, using ARPES, we show that Weyl fermions emerge already in the paramagnetic (PM) phase of $EuCd_2As_2$. Together with measurements of transport, magnetic susceptibility, electron spin resonance (ESR), and muon spin relaxation (μSR) and with first-principles calculations, we attribute the existence of these Weyl fermions to the effective breaking of T symmetry by ferromagnetic (FM) fluctuations on time and length scales that are long compared to the electronic ones, although the spontaneous T symmetry is preserved in the PM phase when considering dynamical statistics.

RESULTS

$EuCd_2As_2$ has a layered crystal structure with space group $P\text{-}3\ m1$ (no. 164). The Cd_2As_2 bilayers are separated by the triangular Eu layers (Fig. 1A). $EuCd_2As_2$ is an itinerant magnet with conduction electrons from the Cd and As orbitals. Magnetism originates from large local magnetic moments on the Eu ions. Previous studies revealed that the local Eu 4*f* moments form a long-range antiferromagnetic (AFM) order with an A-type structure, i.e., FM *a*-*b* planes stacking antiferromagnetically along the *c* axis. This order sets in at the Néel temperature T_N of ~9.5 K (*24*–*26*), at which both the resistivity $\rho(T)$ (Fig. 1A) and the magnetic susceptibility $\chi(T)$ (Fig. 1C) show a peak.

Above T_N, the longitudinal field (LF) μSR spectra show no obvious changes and no oscillations when different magnetic fields are applied in the PM phase of $EuCd_2As_2$ (Fig. 1G). In agreement with previous Mössbauer spectroscopy (*24*), the LF μSR results rule out any static magnetic order above T_N. Nevertheless, ESR measurements reveal that the resonance field (H_{Res}) starts to decrease around 100 K (Fig. 1E),

[1]Swiss Light Source, Paul Scherrer Institute, CH-5232 Villigen PSI, Switzerland. [2]Institute of Condensed Matter Physics, École Polytechnique Fédérale de Lausanne, CH-10 15 Lausanne, Switzerland. [3]Department of Materials Science and Engineering, Stanford University, Stanford, CA 94305, USA. [4]Beijing National Laboratory for Condensed Matter Physics and Institute of Physics, Chinese Academy of Sciences, Beijing 100190, China. [5]School of Physics, University of Chinese Academy of Sciences, Beijing 100190, China. [6]Laboratory for Multiscale Materials Experiments, Paul Scherrer Institute, CH-5232 Villigen PSI, Switzerland. [7]Songshan Lake Materials Laboratory, Dongguan, Guangdong 523808, China. [8]Anhui Province Key Laboratory of Condensed Matter Physics at Extreme Conditions, High Magnetic Field Laboratory, Chinese Academy of Sciences, Hefei, Anhui 230031, China. [9]University of Science and Technology of China, Hefei, Anhui 230026, China. [10]Collaborative Innovation Center of Advanced Microstructures, Nanjing 210093, China. [11]Wuhan National High Magnetic Field Center and School of Physics, Huazhong University of Science and Technology, Wuhan 430074, China. [12]Physikalisches Institut, Karlsruhe Institute of Technology, 76131 Karlsruhe, Germany. [13]Laboratory for Solid State Physics, ETH Zürich, CH-8093 Zürich, Switzerland. [14]Faculty of Physics, Center for Computational Materials Science, University of Vienna, A-1090 Vienna, Austria. [15]Dipartimento di Fisica e Astronomia, Università di Bologna, 40127 Bologna, Italy. [16]Condensed Matter Theory Group, Paul Scherrer Institute, CH-5232 Villigen PSI, Switzerland. [17]Institute of Physics, Ecole Polytechnique Federale de Lausanne, CH1015 Lausanne, Switzerland. [18]CAS Center for Excellence in Topological Quantum Computation, University of Chinese Academy of Sciences, Beijing 100190, China.
*These authors contributed equally to this work.
†Corresponding author. Email: ming.shi@psi.ch (M.Sh.); tqian@iphy.ac.cn (T.Q.); ygshi@iphy.ac.cn (Y.G.S.)

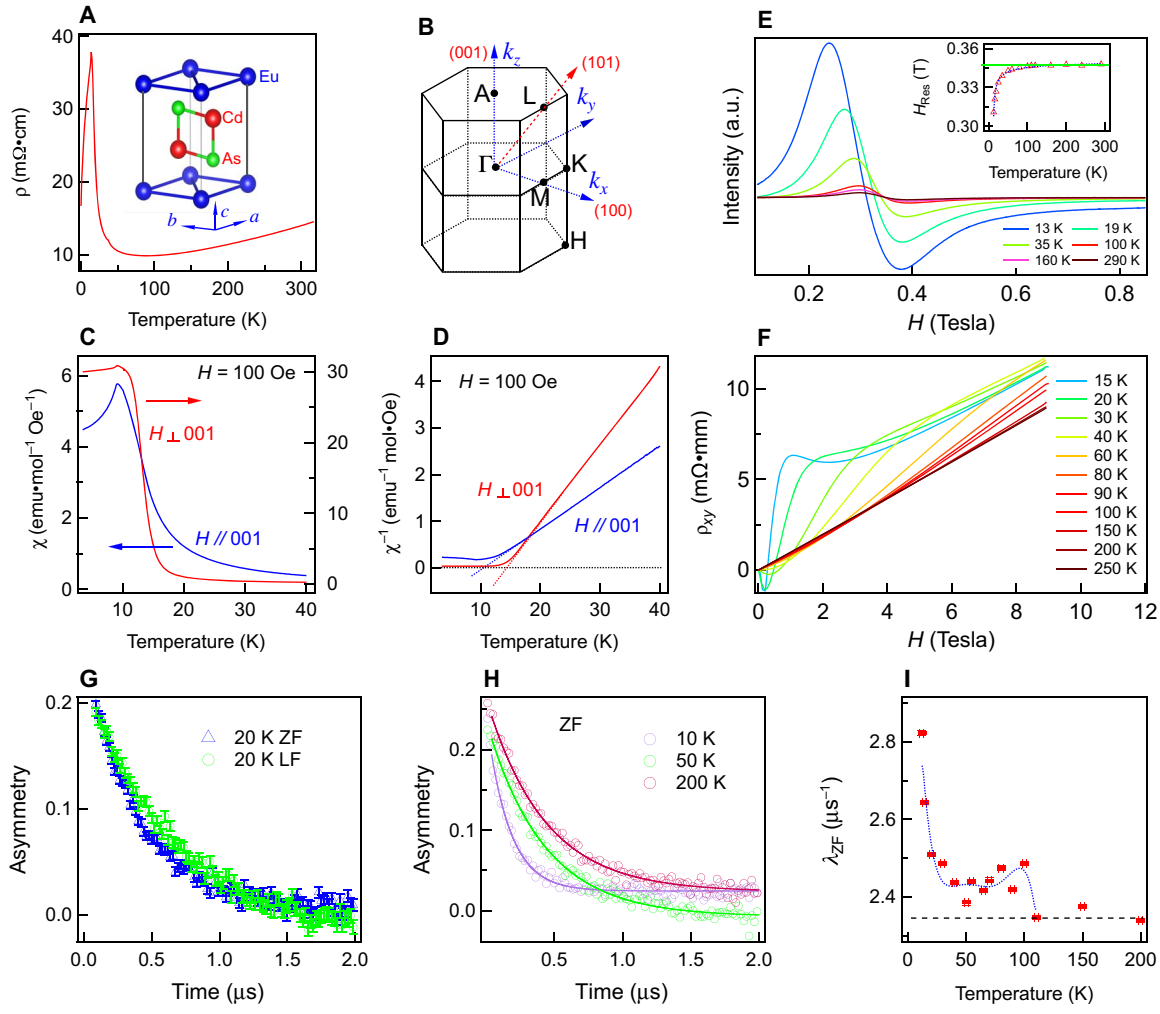

Fig. 1. Slow FM fluctuations in the PM phase of $EuCd_2As_2$. (**A**) Temperature dependence of the resistivity. The inset shows the crystal structure of $EuCd_2As_2$ in one unit cell. mΩ, milliohm. (**B**) 3D Brillouin zone (BZ) with high-symmetry points and coordinate axes. The normal directions of cleaved (001) and (101) surfaces are also indicated. (**C**) Temperature dependence of the magnetic susceptibility with *H* parallel and perpendicular to the *c* axis, respectively. emu, electromagnetic unit. (**D**) Temperature dependence of the inverse susceptibility. (**E**) ESR spectra at various temperatures in the PM phase. The inset plots temperature dependence of the resonance field H_{Res}. a.u., arbitrary units. (**F**) Magnetic field dependence of the Hall resistivity at various temperatures under in-plane magnetic fields. (**G**) μSR spectra at 20 K in zero field (ZF) and longitudinal field (LF) of 7000 Oe, respectively. (**H**) μSR spectra at three representative temperatures. (**I**) Temperature dependence of the dynamic muon relaxation rate λ_{ZF}.

indicating that (i) an effective internal magnetic field develops as the magnetic fluctuations slow down (*27*) and (ii) there is a relatively large scale for the magnetic interactions, most likely associated with strong coupling in the *a*-*b* plane. However, the $\chi^{-1}(T)$ curves exhibit positive but much lower Curie-Weiss temperatures T_{CW} of the same order as T_N, both for magnetic fields (*H*) applied in the *a*-*b* plane or along the *c* axis (Fig. 1D), in agreement with previous measurements (*24*, *25*). The positivity of T_{CW} suggests that magnetic fluctuations above T_N are FM in nature, whereas its smallness as compared to the fluctuation temperature hints at the presence of competing interactions of either sign. Figure 1D shows that there is a crossing between the out-of-plane and the in-plane susceptibilities, with the out-of-plane one being substantially larger at higher temperatures. Together, this suggests predominantly FM fluctuations with out-of-plane magnetization deep in the PM phase.

Further evidence for the existence of a high characteristic temperature scale T_F where fluctuations set in is found in transport. Figure 1F shows that an anomalous Hall effect (AHE) already develops in the PM phase around 100 to 150 K. At temperatures above 150 K, the Hall resistivity exhibits a simple linear dependence on the magnetic field. In contrast, it deviates from the linear behavior when the temperature is below ~100 K. This is also an indication for the onset of quasi-static and quasi–long-range FM correlations at a fairly high T_F because an AHE is typically related to either FM correlations or a nontrivial Berry curvature, associated with Weyl points. However, in the present contest, the latter requires an effective time-reversal symmetry breaking in the form of slow, large-scale FM fluctuations (*28*–*30*).

μSR is one of the most sensitive experimental methods to detect correlated fluctuating local magnetic fields (*31*–*34*) as one would expect from FM fluctuations in the present case. The ensuing exponential muon relaxation is indeed observed in zero field (ZF) and LF at different temperatures (Fig. 1, G and H). When lowering the temperature, the dynamical muon relaxation rate λ_{ZF}, which is related to the fluctuating magnetic field, increases, starting at ~100 K. It then goes through a shoulder between 50 and 100 K and increases more steeply thereafter around T_N (Fig. 1I).

Because of the layered crystal structure, the in-plane magnetic interactions are expected to be much stronger than the interlayer magnetic interactions. This expectation is confirmed qualitatively by the following first-principles calculations. When the measured lattice constants are imposed in the calculation, the ratio between the FM intraplane and AFM interplane nearest-neighbor magnetic exchange couplings is estimated to be of order three in magnitude. We also find a substantial frustration between nearest- and next nearest–neighbor magnetic exchange couplings. However, because the magnitude of these exchange couplings and even the sign of the interplane coupling change when the crystalline structure is allowed to relax during the calculation, a reliable quantitative prediction of their values is very difficult. The small experimental value of the ratio T_N/T_F of ~0.1 also suggests sizable frustration among the competing in-plane magnetic interactions, with the dominant one being FM and of order T_F. FM fluctuations in the plane may thus occur at temperatures below T_F. Once these quasi-static and quasi–long-range magnetic correlations with a magnetization pointing out of plane are established in the Eu planes by strong FM in-plane interactions, dipolar interactions will then further stabilize FM correlations out of the plane. True long-range FM order will, however, be prevented if, upon further cooling, the preferred magnetization changes from an out-of-plane to an in-plane orientation, in which case both dipolar and AFM interlayer exchange interaction prefer an A-type AFM magnetic structure. Such a change of in-plane magnetization direction is exactly what is observed in Fig. 1D where the in-plane susceptibility starts dominating over the out-of-plane susceptibility below 17 K. This is consistent with recent resonant elastic x-ray scattering measurements, which have confirmed that the magnetic moments lie in the *a*-*b* plane below T_N (*26*).

If above T_N a typical FM fluctuation is correlated over a characteristic linear size ξ and over the characteristic time τ such that their inverses exceed the momentum and energy resolution needed to discern the lifting of the Bloch band degeneracy that is expected within the Born-Oppenheimer approximation because of the quasi-static FM, then it will have a measurable effect on the itinerant electrons. In ARPES experiments, we observed the splitting of energy bands in the PM phase of $EuCd_2As_2$. In Fig. 2, we present the ARPES results acquired on cleaved (001) and (101) surfaces of $EuCd_2As_2$ crystals. Figure 2 (A and B) shows a point-like Fermi surface (FS) at the Γ point and cone-like band dispersions below the Fermi level (E_F). In Fig. 2 (C, D, and H), we display

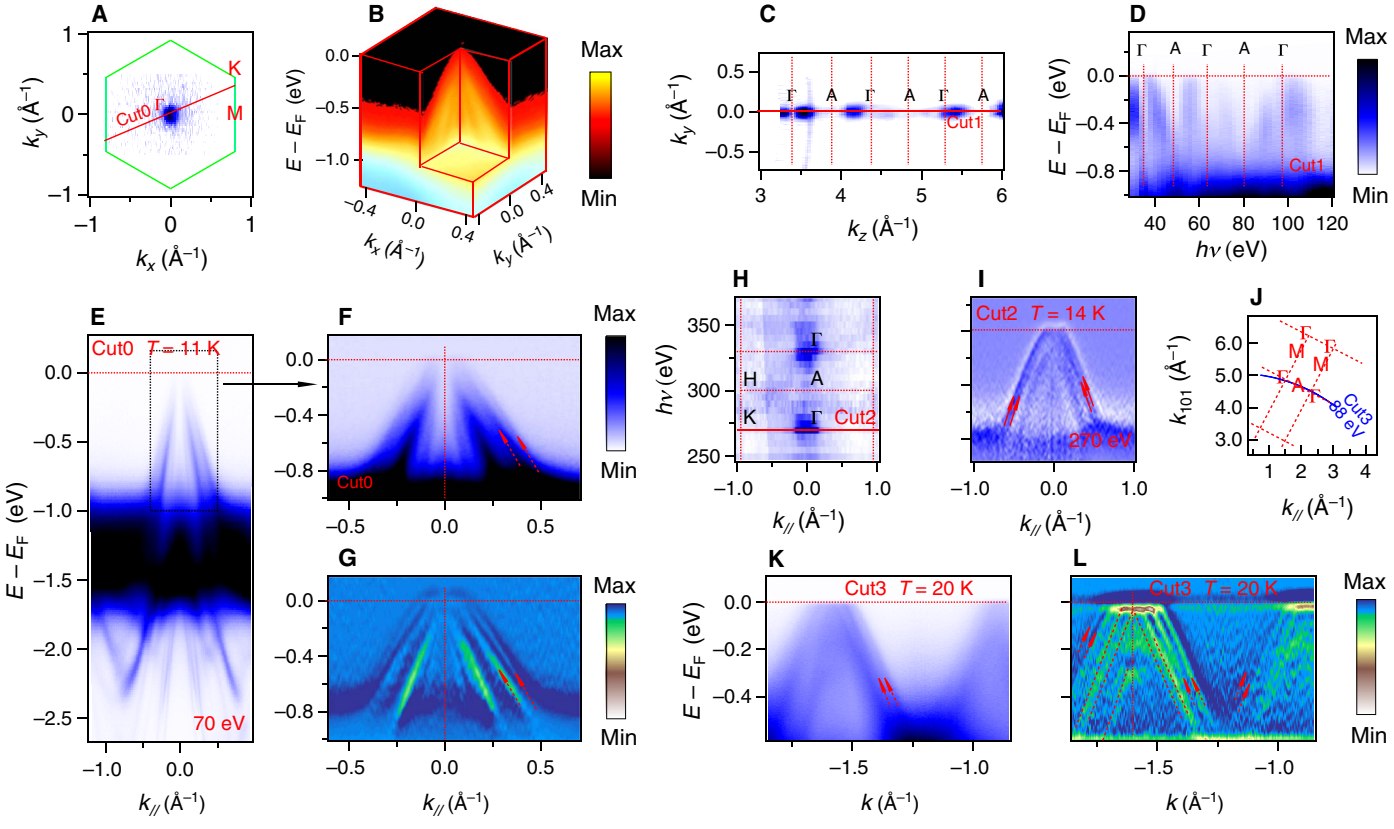

Fig. 2. Band splitting in the PM phase of $EuCd_2As_2$. The ARPES data in (A) to (J) were taken from the cleaved (001) surface, and the data in (K) and (L) were collected from the cleaved (101) surface. (**A**) ARPES intensity map at E_F acquired with photon energy of 70 eV, showing a point-like FS in the k_x-k_y plane. (**B**) 3D intensity plot of the ARPES data collected with $hν$ = 70 eV, showing cone-shaped dispersions in the k_x-k_y plane. (**C**) Intensity plot of the ARPES data at E_F collected with $hν$ varying from 30 to 130 eV, showing the FSs in the k_y-k_z plane. (**D**) ARPES spectrum image along cut1 in the Γ-A direction, as shown in (C). (**E**) A detailed view of the band structure along cut0, as shown in (A), collected at T = 11 K. (**F** and **G**) Zoomed-in views of the raw ARPES spectra in the box shown in (E) and the corresponding 2D curvature intensity plot, respectively. (**H**) Intensity plot of the ARPES data at E_F collected with $hν$ varying from 250 to 360 eV, showing the FSs in the k_y-k_z plane. (**I**) Curvature intensity plot of the ARPES data along Γ-K [cut2 in (H)] collected at T = 14 K with $hν$ = 270 eV. (**J**) The profile of BZs in the plane along normal direction passing through Γ, A, and M points and perpendicular to the (101) surface. (**K** and **L**) The ARPES spectrum and corresponding 2D curvature intensity plot along cut3 in (J). The arrows indicate the band splitting.

the FS in the k_y-k_z plane and band dispersions along the Γ-A line, which is normal to the (001) cleavage surface. The periodic appearance of the FS and the dispersive feature of the energy bands along Γ-A show that they are three-dimensional (3D) bulk states. Figure 2E shows the band dispersions measured at 11 K along cut0 in Fig. 2A: There are flat bands located at ~1 to 1.6 eV below E_F and several hole-like bands above or below the flat bands. While the flat bands arise from the Eu 4*f* orbitals, the hole-like bands mainly originate from the As 4*p* orbits. As the unit cell of $EuCd_2As_2$ contains two As atoms, in total, there are six As 4*p* bands when both *T* and *P* symmetries are preserved. The interlayer coupling within the Cd_2As_2 bilayer results in three antibonding bands around E_F and three bonding bands below the flat bands. Carefully examining the band dispersions, it can be seen that a band splitting occurs near E_F, as indicated by the arrows in Fig. 2 (F and G). To exclude the possibility that the band splitting results from surface effects or the broadening effect of the 3D bulk bands in the photoemission process, we have carried out soft x-ray ARPES measurements to increase the bulk sensitivity in the PM phase (Fig. 2, H and I). The band splitting is still observed in the k_x-k_y plane (Fig. 2I), providing evidence that it is an intrinsic effect of bulk states (*35*). We have also carried out ARPES measurements on the (101) surface. The APRES spectra in Fig. 2 (K and L) were recorded with a photon energy of 88 eV. The corresponding momentum cut almost overlaps with the Γ-A line near the Γ point (Fig. 2J). Note that the band splitting is observed both in the raw ARPES spectra and in the curvature intensity plot, as indicated by the arrows in Fig. 2 (K and L).

Usually, band splitting occurs when either *T* or *P* symmetry is broken. Because both *T* and *P* symmetries are preserved in the PM phase of $EuCd_2As_2$ when considering dynamical statistics over a large enough time scale, we attribute the observed band splitting to slow FM fluctuations with significant spatial correlations, both in plane and out of plane. If the FM fluctuations are much slower than the relevant dynamical time for the itinerant electrons, then a Born-Oppenheimer approximation by which magnetic fluctuations are treated as time-independent background fields for itinerant electrons is justified. A lower bound on the fluctuation time τ for the Born-Oppenheimer approximation to be justified is given by $\hbar/\Delta E_{split}$, with the magnetically induced band splitting ΔE_{split} of ~0.1 eV. This bound is well satisfied because the slow magnetic fluctuations could indeed be detected by μSR (with time resolution larger than picoseconds), which implies that $\tau \gg \hbar/\Delta E_{split}$. The effects of these slow fluctuations can thus be resolved in the spectral functions.

To provide further evidence that the band splitting is induced by spin fluctuations, we have performed ARPES experiments on related compounds in the same family and with the same crystal structure, one magnetic ($EuCd_2Sb_2$) and one nonmagnetic ($BaCd_2As_2$). $EuCd_2Sb_2$ has magnetic properties (such as an AFM phase transition at low temperature and spin fluctuations in the PM phase) very similar to $EuCd_2As_2$, except a slightly lower Néel temperature of ~7.5 K (*24*). The band splitting is very clear in $EuCd_2Sb_2$, as recorded with both an ultraviolet source and soft x-ray ARPES as shown in fig. S1. It persists with increasing temperature up to 100 K, above which the splitting cannot be well resolved (fig. S2). In contrast, we did not observe any band splitting in $BaCd_2As_2$ (fig. S3). We also confirm that the band structure above T_N is very different from that in the low-temperature AFM phase, where a band folding occurs. We provide the associated experimental and numerical data in fig. S4.

To study the band splitting in the PM phase of $EuCd_2As_2$, we have incorporated static FM patterns in our band structure calculations, assuming that fluctuations are much slower than the relevant dynamical time for the itinerant electrons. We carried out density functional theory (DFT) + *U* calculations with infinitude long-range FM order (assuming a large correlation length ξ), with the magnetic moments oriented in various directions. Here, *U* represents the Hubbard interaction among the Eu 4*f* orbitals. For simplicity, we start the discussion with the magnetic moments oriented along the *c* axis. When $U = 0$, a number of flat bands associated with the Eu *4f* orbitals appear near E_F in fig. S5A. Upon increasing *U*, the flat bands move downward as shown in fig. S5 (B to I). For $U = 5$ eV, the flat bands appear at ~1 to 1.6 eV below E_F in Fig. 3A, in agreement with our ARPES results in Fig. 2E. In addition, the calculated band structures at $U = 5$ eV include several hole-like bands above and below the flat bands, which are consistent with the observation in Fig. 2. For comparison, the calculated band structure of $EuCd_2As_2$ in the absence of magnetic order is shown in fig. S6. In this case, the six As 4*p* bands collapse into three doubly degenerate hole-like bands protected by parity-time symmetry.

From our band structure calculations, one can see that the Cd 5*s* and As 4*p* states partially hybridize near E_F for all values of *U*. However, when $U < 5$ eV, because of hybridization with the Eu 4*f* bands, the region near the Fermi level becomes rather tangled, as is seen in fig. S5. For $U \geq 5$ eV instead, an ideal band inversion develops near the Fermi level around the Γ point. This results in an ideal band crossing of the Nth and (N + 1)th bands at $k_z = \pm k_z^c$ on the Γ-A line in the presence of C_{3z} symmetry, as shown in Fig. 3B. In any other k_x-k_y planes with $k_z \neq \pm k_z^c$, the electronic structures are gapped at E_F, which makes it possible to define a Chern number *C* for these planes. We found $C = -1$ for the planes with $|k_z| < k_z^c$ and $C = 0$ for the planes with $|k_z| > k_z^c$. Therefore, the band crossing points along the Γ-A line are topologically protected Weyl nodes. Band crossings resulting in Weyl points can also occur for the (N − 1)th and Nth bands and/or the (N + 1)th and (N + 2)th bands. However, those Weyl nodes are typically farther away from E_F and thus are less relevant for transport. Moreover, they are rather fragile because of the small band inversion and can disappear through pairwise annihilation upon small changes of lattice parameters. Therefore, we focus on the lowest energy pair of Weyl nodes.

When considering FM fluctuations, for the theoretical modeling, we make the following simplifying assumptions: (i) At any given time in the PM phase, the system can be divided into FM correlation domains. (ii) Within each of these domains, the magnetic moments point in the same direction, whereby the orientation in different domains is random and uniformly distributed. (iii) We assume the correlation length to be sufficiently large so that it does not introduce a significant uncertainty in *k* space. Then, the FM fluctuations in the PM phase are captured by averaging the spectra of infinite large FM domains over the magnetic orientations. The resulting band structure along high-symmetry lines is shown in Fig. 3D. The average over directions preserves the band inversion around the Γ point and merely broadens the band structure by an amount W_f (around 0.033 ±0.024 $Å^{-1}$ along M-Γ-K and around 0.024 ±0.012 $Å^{-1}$ along Γ-A). W_f is significantly smaller than the band splitting W_s (0.12±0.02 $Å^{-1}$ along M-Γ-K and 0.086 ±0.030 $Å^{-1}$ along Γ-A), which can thus still be distinguished, as shown in Fig. 3E. The spin splitting W_s observed in ARPES measurements is around 0.066 $Å^{-1}$ along $k_z = 0$ plane and 0.033 $Å^{-1}$ along Γ-A and thus is of the same order of magnitude. The agreement with predicted values is reasonable, given that the above calculation neglects several sources of fluctuations and thus provides at best an upper bound for W_s. The effects of finite correlation lengths of the slow magnetic fluctuations on the visibility of the spin splitting are discussed in the "Spin splitting and band broadening by

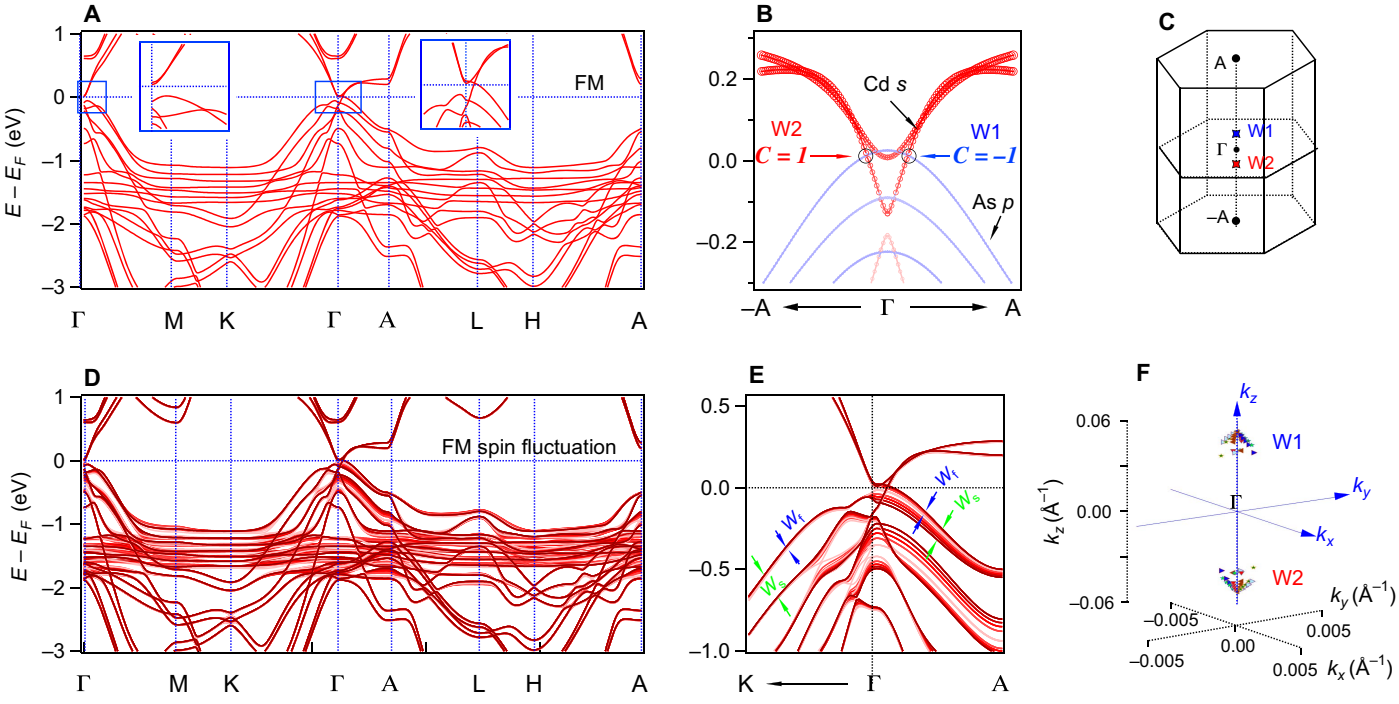

Fig. 3. The band structures in the FM phase and PM phase with FM fluctuations. (**A**) The band structure along high-symmetry lines calculated by using DFT + *U*, with *U* = 5 eV. The magnetic moments oriented in the (001) direction. The insets are the zoomed-in views of band dispersions in the vicinity of the E_F around the Γ point. (**B**) In the near E_F region, the bands along Γ-A with blue and red colors scaling the components of As 4*p* and Cd 5*s* orbitals, respectively. The black circles indicate different Weyl points. (**C**) Locations of Weyl points (W1 and W2) in the 3D BZ. (**D**) The same as that in (A), but the electronic structure is a superposition of the energy bands calculated with the magnetic moments in all possible directions to simulate the FM fluctuation. (**E**) The zoomed-in view of the superposed electronic structure along K-Γ-A in the vicinity of E_F, indicating the broadening effect induced by spin fluctuation. W_s and W_f are width of spin splitting and the band broadening induced by the FM fluctuation, respectively. (**F**) The distribution of Weyl points (W1 and W2) calculated with the magnetic moments oriented in all kinds of typical directions.

static disorder with finite correlation length" section in the Supplementary Text and figs. S7 and S8.

The variation of the location of the Weyl nodes upon changing the magnetic polarization direction in a correlation volume is moderate (see also table S1). For polarization along the *c* axis, the C_{3z} symmetry forces the Weyl nodes to lie on the high-symmetry Γ-A line. For different polarizations, they only deviate slightly from the Γ-A line. As illustrated in Fig. 3F, the pairs of parity-related Weyl nodes are confined in two small nonoverlapping regions around the Γ-A line and the size of each region is less than 0.02 $Å^{-1}$, so the Weyl nodes in the PM phase of $EuCd_2As_2$ can be well detected despite fluctuations of the magnetic polarization direction.

According to the calculations, the separation of the Weyl nodes along the k_z direction is about 0.1 $Å^{-1}$, which is difficult to resolve in the ARPES spectra acquired from the measurements on the (001) surface because of the intrinsic low momentum resolution in the direction perpendicular to the surface. We thus carried out ARPES measurements on cleaved (101) surfaces, whose normal direction is along Γ-L (Fig. 1B). Figure 4A displays the FS intensity map measured from the cleaved (101) surface by varying the photon energy ($h\nu$). The momentum cut corresponding to $h\nu$ = 88 eV almost coincides with the Γ-A-Γ line (Fig. 4A). The 3D ARPES intensity plot acquired at $h\nu$ ~ 88 eV exhibits two separate FS patches along the Γ-A direction (Fig. 4, B and C) with cone-like band dispersions below E_F, in agreement with the calculations. To get an ARPES spectrum exactly on the Γ-A line, we collected a large set of ARPES data with photon energies in the vicinity of 88 eV. Figure 4D shows the band dispersions along Γ-A extracted from the photon energy–dependent data, which has much better momentum resolution than that measured on the (001) surface along the same direction (Fig. 2D). The band splitting of the hole-like band can be identified both in the raw data and in the curvature intensity plot (Fig. 4, D and E). In addition, we observed a shallow electron-like band [conduction band (CB)] near E_F (Fig. 4, F and H). As indicated in Fig. 4 (F, H, and I, the electron- and hole-like bands, marked as CB and valence band (VB), respectively, cross E_F. As the electron band is also spin nondegenerate, the crossings of the Nth and (N + 1)th bands lead to a pair of Weyl nodes around Γ-A, with k_z of ~±0.07 $Å^{-1}$. To further confirm the crossings of CB and VB, we carried out scanning tunneling microscopy/spectroscopy (STM/STS) measurements on the (001) surface (Fig. 4, J and K). The typical d*I*/d*V* spectrum in Fig. 4K exhibits a "V" shape with a finite minimal intensity at E_F and shows peaks both above and below E_F, which agree well with the inverted VB top (VBT) and CB bottom (CBB), as marked in Fig. 4I. This is in agreement with the expected density of states of a Weyl cone band structure.

In addition to the bulk Weyl nodes, a further important feature of WSMs is surface Fermi arcs. On the (101) cleaved surface, the two Weyl nodes are projected to different points in the surface Brillouin zone (BZ), which should be connected by a surface Fermi arc. We indeed observe a signature of surface states in the photon energy–dependent spectra and in the FS map. However, the Fermi arcs are rather sensitive to fluctuations of the polarization direction, which entails an intrinsic smearing of these surface states between the two Weyl points.

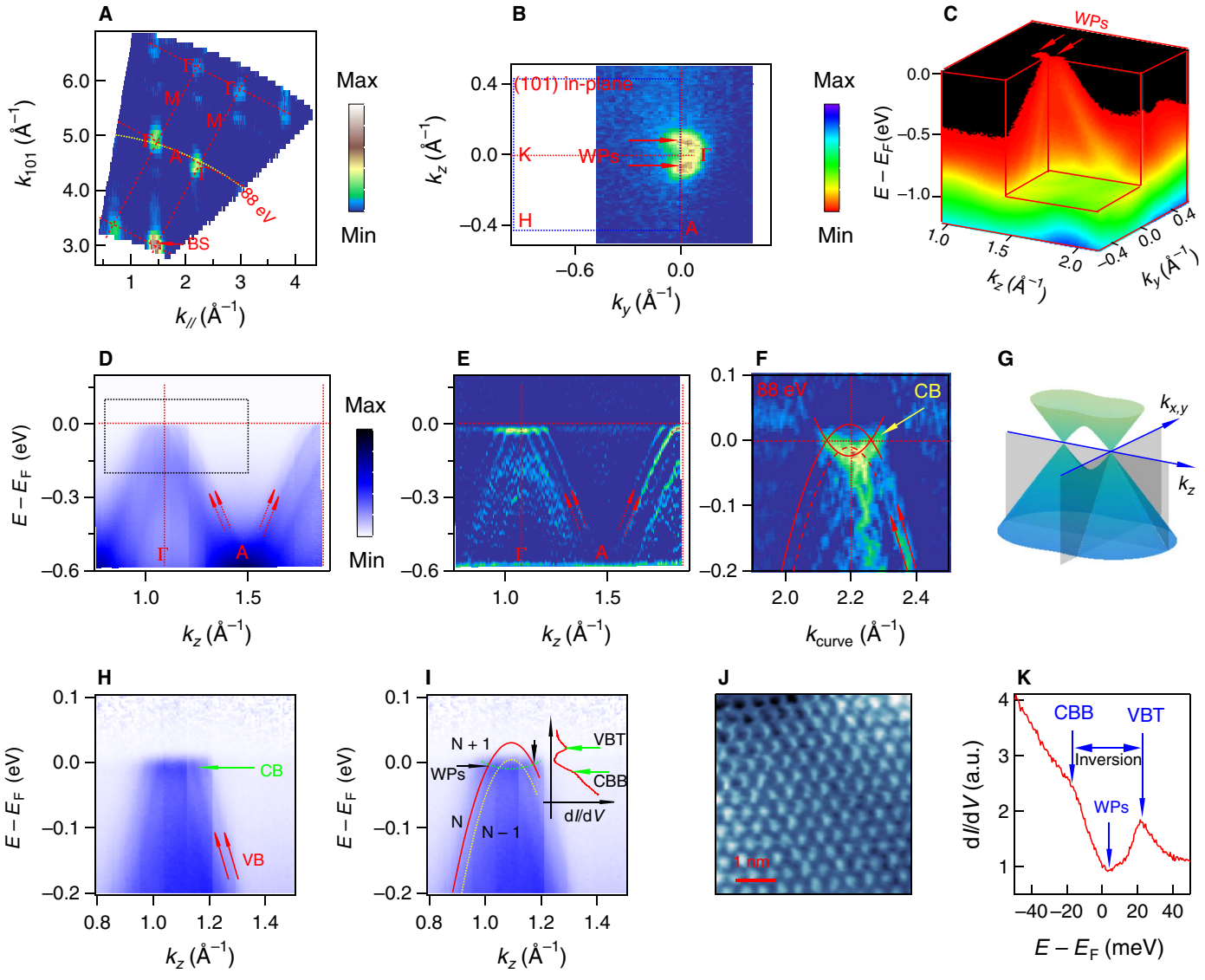

Fig. 4. The observation of Weyl cones. Unless otherwise mentioned, the spectra are collected from the cleaved (101) surface using $h\nu$ = 88 eV, and the corresponding momentum cut is indicated with the yellow curve in (A), which almost overlaps with the Γ-A-Γ line. (**A**) The FS map in the k_x-k_z plane, collected with $h\nu$ in the range of 30 to 160 eV. BS, bulk states. (**B**) The FS map in the k_y-k_z plane. (**C**) The 3D ARPES intensity to show two point-like FSs on Γ-A and the cone-shaped dispersions in the k_y-k_z plane. WPs, Weyl points. (**D** and **E**) The ARPES spectrum and its corresponding curvature intensity plot along Γ-A. To obtain the ARPES spectrum on a straight line located exactly on the Γ-A line, a number of high-resolution ARPES data were collected with photon energies in the vicinity of 88 eV. The arrows indicate the band splitting. (**F**) The 2D curvature intensity plot of the ARPES spectrum along the yellow curve in (A). An electron CB with band bottom below E_F is visible. (**G**) Schematic of the 3D Weyl cone band structure in the k_x-k_z (k_y-k_z) plane. (**H** and **I**) Zoomed-in views of the dashed line box in (D); the spectrum was divided by Fermi-Dirac function. In (I), black arrows point to the Weyl points. The tunneling differential conductance (d*I*/d*V*) curve from STS measurements is plotted for comparison. (**J**) STM constant current topographic image obtained from (001) surface of $EuCd_2As_2$. (**K**) The d*I*/d*V* spectrum recorded at T = 11 K on the (001) surface. In this figure, the data in (A) to (C) and (F) [(D) to (E) and (H) to (I)] were collected from sample no. 1 (sample no. 2). We note that sample no. 1 is slightly less hole-doped than sample no. 2, which makes the electron band easier to be explored in sample no. 1 in (F).

DISCUSSION AND CONCLUSION

We have shown that the Bloch bands of $EuCd_2As_2$ display topological attributes in the form of Weyl nodes that originate from the interplay between itinerant electrons and localized moments in the PM phase below the crossover temperature of ~100 K. Far above 100 K, the Weyl nodes collapse into Dirac nodes as the typical lifetime or the spatial extent of the FM fluctuations becomes too short for the Kramers' degeneracy to be effectively broken. None of the probes used in this paper have direct access to the magnetic coupling of order 100 K that is responsible for the long-lived FM fluctuations. The observation of Weyl nodes in $EuCd_2As_2$ is thus to be interpreted as the imprint on the Bloch bands of rather large competing magnetic interactions of the order of 100 K.

Note that the time scale for collecting ARPES spectra is much longer than that of the spin fluctuations. Therefore, ARPES data can be viewed as a statistical time average of dynamical results. The spin fluctuations

do have an effect on the electronic structure, as they induce fluctuations on the Weyl nodes and the sign of the topological charge in the two Weyl node groups. These kinds of fluctuations, in Weyl node and charge sign, are sensitive to the magnetization, which can be tuned by an external magnetic field. The fact that Weyl nodes and their topological charge adjust to the orientation of the magnetization, which is itself tunable, could be promising for future spintronic applications.

A recent theoretical study has pointed out that a Dirac semimetal state or magnetic topological insulator state could coexist under certain conditions with long-range AFM order (*36*). If this is also true for $EuCd_2As_2$ below T_N, then the application of moderate magnetic fields could induce a metamagnetic transition to an FM state that would very substantially split the Kramers' degeneracy even for a moderate field. We thus expect the phase diagram of $EuCd_2As_2$ as a function of temperature and magnetic field to be very rich.

MATERIALS AND METHODS

Single crystals of $EuCd_2As_2$ were synthesized using Sn as flux. Starting materials of Eu (ingot, 99.9%), Cd (grain 99.999%), As (ingot, 99.999%), and excess Sn (grain, 99.9969%; all from Alfa Aesar) were mixed and loaded in an alumina crucible at a molar ratio of 1:2:2:10. The operations were performed in a glove box filled with pure argon. Then, the crucible was sealed in a quartz tube under high vacuum. The tube was heated to 900°C and maintained for 20 hours before slowly cooling it to 500°C at a rate of 2°C/hour. Then, the samples were separated from the Sn in a centrifuge.

ARPES measurements were performed at the SIS-HRPES (Surface And Interface Spectroscopy–High-Resolution Photoemission Spectroscopy) beamline with a Scienta R4000 analyzer and at the ADRESS (ADvanced RESonant Spectroscopies) beamline with a SPECS analyzer of the Swiss Light Source [Paul Scherrer Institute (PSI)], at the ARPES end station of the Dreamline beamline at the Shanghai Synchrotron Radiation Facility and at the beamline UE112 PGM-2b-1^3 at BESSY (Berlin Electron Storage Ring Society for Synchrotron Radiation) Synchrotron. The energy and angular resolutions were set to ~5 to 30 meV and 0.2°, respectively. The samples for ARPES measurements were cleaved in situ and measured in a temperature range between 2 and 160 K in a vacuum better than 5×10^{-11} torr. The μSR measurements were carried out using the general purpose spectrometers located at the πM3 beamline of the Swiss Muon Source of the PSI. STM measurements were carried out with a home-built Joule-Thomson STM (*37*). The $EuCd_2As_2$ single crystals were cleaved in situ at $T = 77$ K. Measurements were performed at $T = 2.8$ to 14 K.

The DFT calculations were carried out by using the projector-augmented wave method implemented in the Vienna ab initio simulation package (VASP) (*38*, *39*). The cutoff energy for the plane-wave expansion was 500 eV. The exchange-correlation functional was treated using the generalized gradient approximation (GGA) parameterized by Perdew *et al*. (*40*). Spin-orbit coupling (SOC) was taken into account self-consistently in the calculations. The k-point grids (10 by 10 by 5) were used in the self-consistent simulations. The GGA + U method (*41*) was used to treat correlation effects in $EuCd_2As_2$. The *s* orbitals of Cd and the *p* orbitals of As were used to construct the maximally localized Wannier functions (*42*), which were then used to calculate the Chern numbers.

To analyze the effects of the magnetic disorder with different FM clustering properties on the energy band structure of EuCd2As2, we carried out DFT + U calculations ($U = 5$ eV), including SOC, by using a supercell (4 by 4 by 1; 80 atoms). The magnetic moments of the 16 Eu atoms were constrained along arbitrary directions, exploring different arrangements. The band structure was unfolded onto the primitive cell BZ by adopting the unfolding method, as implemented in VASP (*43*, *44*).

SUPPLEMENTARY MATERIALS

Supplementary material for this article is available at http://advances.sciencemag.org/cgi/content/full/5/7/eaaw4718/DC1

Spin splitting and band broadening by static disorder with finite correlation length

Fig. S1. Band splitting in $EuCd_2Sb_2$.

Fig. S2. Temperature effects on the band splitting in $EuCd_2Sb_2$.

Fig. S3. Electronic structure of $BaCd_2As_2$.

Fig. S4. Comparison of band structures below and above Néel temperature.

Fig. S5. Calculated band structures of $EuCd_2As_2$ with magnetic moments oriented along the *c* axis, as a function of onsite Coulomb interaction U.

Fig. S6. Calculated band structure of $EuCd_2As_2$ along high-symmetry lines, deeply within the PM phase.

Fig. S7. Band structures with different magnetic backgrounds differing in size of FM clusters.

Fig. S8. The mean free path as a function of the FM correlation length.

Table S1. Positions of the Weyl points in $EuCd_2As_2$ depending on the spin orientation.

REFERENCES AND NOTES

1. Z. Wang, Y. Sun, X.-Q. Chen, C. Franchini, G. Xu, H. Weng, X. Dai, Z. Fang, Dirac semimetal and topological phase transitions in A_3Bi (A=Na, K, Rb). *Phys. Rev. B* **85**, 195320 (2012).
2. Z. K. Liu, B. Zhou, Y. Zhang, Z. J. Wang, H. M. Weng, D. Prabhakaran, S. K. Mo, Z. X. Shen, Z. Fang, X. Dai, Z. Hussain, Y. L. Chen, Discovery of a three-dimensional topological dirac semimetal Na_3Bi. *Science* **343**, 864–867 (2014).
3. Z. Wang, H. Weng, Q. Wu, X. Dai, Z. Fang, Three-dimensional Dirac semimetal and quantum transport in Cd_3As_2. *Phys. Rev. B* **88**, 125427 (2013).
4. Z. K. Liu, J. Jiang, B. Zhou, Z. J. Wang, Y. Zhang, H. M. Weng, D. Prabhakaran, S. K. Mo, H. Peng, P. Dudin, T. Kim, M. Hoesch, Z. Fang, X. Dai, Z. X. Shen, D. L. Feng, Z. Hussain, Y. L. Chen, A stable three-dimensional topological Dirac semimetal Cd_3As_2. *Nat. Mater.* **13**, 677–681 (2014).
5. X. Wan, A. M. Tuner, A. Vishwanath, S. Y. Savrasov, Topological semimetal and Fermi-arc surface states in the electronic structure of pyrochlore iridates. *Phys. Rev. B* **83**, 205101 (2011).
6. G. Xu, H. Weng, Z. Wang, X. Dai, Z. Fang, Chern semimetal and the quantized anomalous Hall effect in $HgCr_2Se_4$. *Phys. Rev. Lett.* **107**, 186806 (2011).
7. H. Weng, C. Fang, Z. Fang, B. A. Bernevig, X. Dai, Weyl semimetal phase in noncentrosymmetric transition-metal monophosphides. *Phys. Rev. X* **5**, 011029 (2015).
8. S.-M. Huang, S. Y. Xu, I. Belopolski, C.-C. Lee, G. Chang, B. K. Wang, N. Alidoust, G. Bian, M. Neupane, C. Zhang, S. Jia, A. Bansil, H. Lin, M. Z. Hasan, A Weyl fermion semimetal with surface Fermi arcs in the transition metal monopnictide TaAs class. *Nat. Commun.* **6**, 7373 (2015).
9. A. A. Soluyanov, D. Gresch, Z. Wang, Q. S. Wu, M. Troyer, X. Dai, B. A. Bernevig, Type-II Weyl semimetals. *Nature* **527**, 495–498 (2015).
10. J. Kübler, C. Felser, Weyl fermions in antiferromagnetic Mn_3Sn and Mn_3Ge. *Euro. Phys. Lett.* **120**, 47002 (2017).
11. B. Q. Lv, H. M. Weng, B. B. Fu, X. P. Wang, H. Miao, J. Ma, P. Richard, X. C. Huang, L. X. Zhao, G. F. Chen, Z. Fang, X. Dai, T. Qian, H. Ding, Experimental discovery of Weyl semimetal TaAs. *Phys. Rev. X* **5**, 031013 (2015).
12. S. Y. Xu, I. Belopolski, N. Alidoust, M. Neupane, G. Bian, C. Zhang, R. Sankar, G. Chang, Z. Yuan, C. C. Lee, S. M. Huang, H. Zheng, J. Ma, D. S. Sanchez, B. Wang, A. Bansil, F. Chou, P. P. Shibayev, H. Lin, S. Jia, M. Z. Hasan, Discovery of a Weyl fermion semimetal and topological Fermi arcs. *Science* **349**, 613–617 (2015).
13. B. Q. Lv, N. Xu, H. M. Weng, J. Z. Ma, P. Richard, X. C. Huang, L. X. Zhao, G. F. Chen, C. E. Matt, F. Bisti, V. N. Strocov, J. Mesot, Z. Fang, X. Dai, T. Qian, M. Shi, H. Ding, Observation of Weyl nodes in TaAs. *Nat. Phys.* **11**, 724–727 (2015).
14. L. X. Yang, Z. K. Liu, Y. Sun, H. Peng, H. F. Yang, T. Zhang, B. Zhou, Y. Zhang, Y. F. Guo, M. Rahn, D. Prabhakaran, Z. Hussain, S.-K. Mo, C. Felser, B. Yan, Y. L. Chen, Weyl semimetals in the non-centrosymmetric compound TaAs. *Nat. Phys.* **11**, 728–732 (2015).
15. L. Huang, T. M. McCormick, M. Ochi, Z. Zhao, M. T. Suzuki, R. Arita, Y. Wu, D. Mou, H. Cao, J. Yan, N. Trivedi, A. Kaminski, Spectroscopic evidence for a type II Weyl semimetallic state in $MoTe_2$. *Nat. Mater.* **15**, 1155–1160 (2016).
16. K. Deng, G. Wan, P. Deng, K. Zhang, S. Ding, E. Wang, M. Yan, H. Huang, H. Zhang, Z. Xu, J. Denlinger, A. Fedorov, H. Yang, W. Duan, H. Yao, Y. Wu, S. Fan, H. Zhang, X. Chen,

S. Zhou, Experimental observation of topological Fermi arcs in type-II Weyl semimetal $MoTe_2$. *Nat. Phys.* **12**, 1105–1110 (2016).
17. S.-Y. Xu, N. Alidoust, G. Chang, H. Lu, B. Singh, I. Belopolski, D. S. Sanchez, X. Zhang, G. Bian, H. Zheng, M. A. Husanu, Y. Bian, S. M. Huang, C. H. Hsu, T. R. Chang, H. T. Jeng, A. Bansil, T. Neupert, V. N. Strocov, H. Lin, S. Jia, M. Z. Hasan, Discovery of Lorentz-violating type II Weyl fermions in LaAlGe. *Sci. Adv.* **3**, e1603266 (2017).
18. I. Belopolski, P. Yu, D. S. Sanchez, Y. Ishida, T. R. Chang, S. S. Zhang, S. Y. Xu, H. Zheng, G. Chang, G. Bian, H. T. Jeng, T. Kondo, H. Lin, Z. Liu, S. Shin, M. Z. Hasan, Signatures of a time-reversal symmetric Weyl semimetal with only four Weyl points. *Nat. Commun.* **8**, 942 (2017).
19. X. Huang, L. Zhao, Y. Long, P. Wang, D. Chen, Z. Yang, H. Liang, M. Xue, H. Weng, Z. Fang, X. Dai, G. Chen, Observation of the Chiral-anomaly-induced negative magnetoresistance in 3D Weyl semimetal TaAs. *Phys. Rev. X* **5**, 031023 (2015).
20. J. Xiong, S. K. Kushwaha, T. Liang, J. W. Krizan, M. Hirschberger, W. Wang, R. J. Cava, N. P. Ong, Evidence for the chiral anomaly in the Dirac semimetal Na_3Bi. *Science* **350**, 413–416 (2015).
21. M. Hirschberger, S. Kushwaha, Z. Wang, Q. Gibson, S. Liang, C. A. Belvin, B. A. Bernevig, R. J. Cava, N. P. Ong, The chiral anomaly and thermopower of Weyl fermions in the half-Heusler GdPtBi. *Nat. Mater.* **15**, 1161–1165 (2016).
22. K. Kuroda, T. Tomita, M. T. Suzuki, C. Bareille, A. A. Nugroho, P. Goswami, M. Ochi, M. Ikhlas , M. Nakayama, S. Akebi, R. Noguchi, R. Ishii, N. Inami, K. Ono, H. Kumigashira, A. Varykhalov, T. Muro, T. Koretsune, R. Arita, S. Shin, T. Kondo, S. Nakatsuji, Evidence for magnetic Weyl fermions in a correlated metal. *Nat. Mater.* **16**, 1090–1095 (2017).
23. E. Liu, Y. Sun, N. Kumar, L. Müchler, A. Sun, L. Jiao, S. Y. Yang, D. Liu, A. Liang, Q. Xu, J. Kroder, V. Süß, H. Borrmann, C. Shekhar, Z. Wang, C. Xi, W. Wang, W. Schnelle, S. Wirth, Y. Chen, S. T. B. Goennenwein, C. Felser, Giant anomalous Hall effect in a ferromagnetic Kagomé-lattice semimetal. *Nat. Phys.* **14**, 1125–1131 (2018).
24. I. Schellenberg, U. Pfannenschmidt, M. Eul, C. Schwickert, R. A. Pöttgen, A ^{121}Sb and ^{151}Eu Mössbauer spectroscopic investigation of $EuCd_2X_2$ (X = P, As, Sb) and $YbCd_2Sb_2$. *Z. Anorg. Allg. Chem.* **637**, 1863–1870 (2011).
25. H.-P. Wang, D. S. Wu, Y. G. Shi, N. L. Wang, Anisotropic transport and optical spectroscopy study on antiferromagnetic triangular lattice $EuCd_2As_2$: An interplay between magnetism and charge transport properties. *Phys. Rev. B* **94**, 045112 (2016).
26. M. C. Rahn, J.-R. Soh, S. Francoual, L. S. I. Veiga, J. Strempfer, J. Mardegan, D. Y. Yan, Y. F. Guo, Y. G. Shi, A. T. Boothroyd, Coupling of magnetic order and charge transport in the candidate Dirac semimetal $EuCd_2As_2$. *Phys. Rev. B* **97**, 214422 (2018).
27. Y. Goryunov, A. Nateprov, Spin and valence fluctuation in Eu compounds with $CaAl_2Si_2$-structure. *JPS Conf. Proc.* **3**, 011026 (2014).
28. N. Nagaosa, J. Sinova, S. Onoda, A. H. MacDonald, N. P. Ong, Anomalous Hall effect. *Rev. Mod. Phys.* **82**, 1539–1592 (2010).
29. S. Nakatsuji, N. Kiyohara, T. Higo, Large anomalous Hall effect in a non-collinear antiferromagnet at room temperature. *Nature* **527**, 212–215 (2015).
30. A. K. Nayak, J. E. Fischer, Y. Sun, B. Yan, J. Karel, A. C. Komarek, C. Shekhar, N. Kumar, W. Schnelle, J. Kübler, C. Felser, S. S. P. Parkin, Large anomalous Hall effect driven by a nonvanishing Berry curvature in the noncolinear antiferromagnet Mn_3Ge. *Sci. Adv.* **2**, e1501870 (2016).
31. G. M. Luke, Y. Fudamoto, K. M. Kojima, M. I. Larkin, J. Merrin, B. Nachumi, Y. J. Uemura, Y. Maeno, Z. Q. Mao, Y. Mori, H. Nakamura, M. Sigrist, Time-reversal symmetry-breaking superconductivity in Sr_2RuO_4. *Nature* **394**, 558–561 (1998).
32. R. P. Singh, A. D. Hillier, B. Mazidian, J. Quintanilla, J. F. Annett, D. M. K. Paul, G. Balakrishnan, M. R. Lees, Detection of time-reversal symmetry breaking in the noncentrosymmetric superconductor Re_6Zr using muon-spin spectroscopy. *Phys. Rev. Lett.* **112**, 107002 (2014).
33. T. Shang, G. M. Pang, C. Baines, W. B. Jiang, W. Xie, A. Wang, M. Medarde, E. Pomjakushina, M. Shi, J. Mesot, H. Q. Yuan, T. Shiroka, Nodeless superconductivity and time-reversal symmetry breaking in the noncentrosymmetric superconductor $Re_{24}Ti_5$. *Phys. Rev. B* **97**, 020502 (2018).
34. J. Zhang, Z. Ding, C. Tan, K. Huang, O. O. Bernal, P. C. Ho, G. D. Morris, A. D. Hillier, P. K. Biswas, S. P. Cottrell, H. Xiang, X. Yao, D. E. MacLaughlin, L. Shu, Discovery of slow magnetic fluctuations and critical slowing down in the pseudogap phase of $YBa_2Cu_3O_y$. *Sci. Adv.* **4**, eaao5235 (2018).
35. V. N. Strocov, M. Shi, M. Kobayashi, C. Monney, X. Wang, J. Krempasky, T. Schmitt, L. Patthey, H. Berger, P. Blaha, Three-dimensional electron realm in VSe_2 by soft-x-ray photoelectron spectroscopy: Origin of charge-density waves. *Phys. Rev. Lett.* **109**, 086401 (2012).
36. G. Hua, S. Nie, Z. Song, R. Yu, G. Xu, K.-L. Yao, Dirac semimetal in type IV magnetic space group. *Phys. Rev. B* **98**, 201116 (2018).
37. L. Zhang, T. Miyamachi, T. Tomanic, R. Dehm, W. Wulfhekel, A compact sub-Kelvin ultrahigh vacuum scanning tunneling microscope with high energy resolution and high stability. *Rev. Sci. Instrum.* **82**, 103702 (2011).
38. G. Kresse, J. Furthmuller, Efficiency of ab-initio total energy calculations for metals and semiconductors using a plane-wave basis set. *Comput. Mater. Sci.* **6**, 15–50 (1996).
39. G. Kresse, J. Furthmüller, Efficient iterative schemes for ab initio total-energy calculations using a plane-wave basis set. *Phys. Rev. B* **54**, 11169–11186 (1996).
40. J. P. Perdew, K. Burke, M. Ernzerhof, Generalized gradient approximation made simple. *Phys. Rev. Lett.* **77**, 3865–3868 (1996).
41. A. I. Liechtenstein, V. I. Anisimov, J. Zaanen, Density-functional theory and strong interactions: Orbital ordering in Mott-Hubbard insulators. *Phys. Rev. B* **52**, R5467–R5470 (1995).
42. N. Marzari, A. A. Mostofi, J. R. Yates, I. Souza, D. Vanderbilt, Maximally localized Wannier functions: Theory and applications. *Rev. Mod. Phys.* **84**, 1419 (2012).
43. P. Liu, M. Reticcioli, B. Kim, A. Continenza, G. Kresse, D. D. Sarma, X.-Q. Chen, C. Franchini, Electron and hole doping in the relativistic Mott insulator Sr_2IrO_4: A first-principles study using band unfolding technique. *Phys. Rev. B* **94**, 195145 (2016).
44. M. Reticcioli, G. Profeta, C. Franchini, A. Continenza, Ru doping in iron-based pnictides: The "unfolded" dominant role of structural effects for superconductivity. *Phys. Rev. B* **95**, 214510 (2017).

Acknowledgments: We acknowledge E. Rienks, H. Luetkens, L.-Y. Kong, Y.-G. Zhong, H.-J. Liu, S.-Y Gao, X.-L Peng, and Y.-B. Huang for the assistance during the measurements. We acknowledge Y. Goryunov, H.-M. Weng, L. Korosec, R. H. Ott, P. Hautle, Q. S. Wu, V. M. Katukuri, and O. Yazyev for useful discussions. C.M. and M.Mü. thank B. Roessli for useful discussions. We acknowledge S. Blundell for sharing the μSR beamtime. **Funding:** This work was supported by the NCCR-MARVEL funded by the Swiss National Science Foundation, the Sino-Swiss Science and Technology Cooperation (grant no. IZLCZ2-170075), the Ministry of Science and Technology of China (grant nos. 2016YFA0300600, 2016YFA0401000, 2017YFA0302901, and 2016YFA0300404), the National Natural Science Foundation of China (grant nos. 11622435, 11474340, 11474330, 11674369, and U1832202), the Chinese Academy of Sciences (grant nos. QYZDB-SSW-SLH043, XDB07000000, XDPB08-1, and XDB28000000), and Beijing Municipal Science & Technology Commission (grant nos. Z171100002017018 and Z181100004218005). This project has received funding from the European Union's Horizon 2020 research and innovation programme under the Marie Skłodowska-Curie grant agreement no. 701647. **Author contributions:** M.Sh., T.Q., and J.-Z.M. supervised this project. J.-Z.M. performed the ARPES measurements with the assistance of M.Y.Y., M.N., A.C., and V.N.S. S.M.N. performed the ab initio calculations with long-range magnetic order background with the help of G.X. M.R. and C.F. performed the band structure in the enlarged unit cell with different magnetic backgrounds that differ in their average magnetization and clustering properties. C.J.Y. and Y.G.S. synthesized the single crystals and performed the resistance and magnetization measurements on single-crystal $EuCd_2As_2$ and $BaCd_2As_2$. M.So. and Y.-M.X. synthesized the single crystal of $EuCd_2Sb_2$. T.S. and J.-Z.M. performed the AHE and μSR measurements. J.J., J.-Z.M., and W.W. performed the STM/STS measurements. L.Q.Y. and Y.S. performed the ESR measurements. J.-Z.M., T.Q., J.J., T.S., and M.Sh. analyzed the experimental data and discussed them with H.D. and J.M. J.-Z.M., T.Q., M.Sh., and M.R. plotted the figures. J.-Z.M., T.Q., M.Sh., M.M., and C.M. wrote the manuscript. All the authors discussed the results. **Competing interests:** The authors declare that they have no competing interests. **Data and materials availability:** All data needed to evaluate the conclusions in the paper are present in the paper and/or the Supplementary Materials. Materials and additional data related to this paper may be requested from the authors.

Submitted 22 December 2018
Accepted 10 June 2019
Published 12 July 2019
10.1126/sciadv.aaw4718

Citation: J.-Z. Ma, S. M. Nie, C. J. Yi, J. Jandke, T. Shang, M. Y. Yao, M. Naamneh, L. Q. Yan, Y. Sun, A. Chikina, V. N. Strocov, M. Medarde, M. Song, Y.-M. Xiong, G. Xu, W. Wulfhekel, J. Mesot, M. Reticcioli, C. Franchini, C. Mudry, M. Müller, Y. G. Shi, T. Qian, H. Ding, M. Shi, Spin fluctuation induced Weyl semimetal state in the paramagnetic phase of $EuCd_2As_2$. *Sci. Adv.* **5**, eaaw4718 (2019).

Spin fluctuation induced Weyl semimetal state in the paramagnetic phase of $EuCd_2As_2$

J.-Z. Ma, S. M. Nie, C. J. Yi, J. Jandke, T. Shang, M. Y. Yao, M. Naamneh, L. Q. Yan, Y. Sun, A. Chikina, V. N. Strocov, M. Medarde, M. Song, Y.-M. Xiong, G. Xu, W. Wulfhekel, J. Mesot, M. Reticcioli, C. Franchini, C. Mudry, M. Müller, Y. G. Shi, T. Qian, H. Ding and M. Shi

Sci Adv **5** (7), eaaw4718.
DOI: 10.1126/sciadv.aaw4718